Low thermal conductivity and high thermoelectric performance via Cd underbonding in half-Heusler PCdNa

Xianfeng Ye,[1] Zhenzhen Feng,[1,*] Yongsheng Zhang,[2,3] Gaofeng Zhao,[1,†] and David J. Singh[4,‡]

[1]*Institute for Computational Materials Science, School of Physics and Electronics, International Joint Research Laboratory of New Energy Materials and Devices of Henan Province, Henan University, Kaifeng 475004, China*

[2]*Science Island Branch of Graduate School, University of Science and Technology of China, Hefei 230026, China*

[3]*Key Laboratory of Materials Physics, Institute of Solid State Physics, Chinese Academy of Sciences, Hefei 230031, China*

[4]*Department of Physics and Astronomy, Department of Mechanical & Aerospace Engineering and Department of Chemistry, University of Missouri, Columbia, Missouri 65211, USA*

(Received 16 January 2022; revised 15 March 2022; accepted 18 March 2022; published 29 March 2022)

Half-Heusler compounds are a very large class of materials that have received attention as promising high-temperature thermoelectric materials due to their favorable electrical transport behavior and other properties beneficial for device fabrication. A particular challenge is that while half-Heusler compounds show an exceptionally large range of thermal conductivities, these are still generally higher than other state-of-the-art thermoelectric materials. Here, we investigate PCdNa, which was reported to be a material that may form in the half-Heusler structure and have an unusually low thermal conductivity. This is in order to understand its very low thermal conductivity and elucidate its electronic properties in relation to thermoelectricity. We find that the low thermal conductivity of 2.6 W/mK at 300 K is a consequence of underbonding of the Cd ions within the network formed by the P. This underbonding leads to anharmonicity and relatively low frequency phonons and may be regarded as a generalized effective rattling phenomenon. The electronic structure shows a high valence band degeneracy, which we find leads to favorable good electrical transport properties. The combination of the low lattice thermal conductivity and favorable electrical transport properties results in high p-type thermoelectric performance. The figure of merit is predicted to reach $ZT = 3.3$ at 900 K for optimum p-type doping. This suggests that PCdNa is a promising p-type high-temperature half-Heusler thermoelectric material.

DOI: 10.1103/PhysRevB.105.104309

I. INTRODUCTION

The decreasing supply of petrochemical fuel and its concomitant environmental pollution are urgent issues in the 21st century. In this regard, thermoelectric (TE) materials, which can convert heat directly into electricity without moving parts or emissions [1], have attracted much interest. However, broad application of TE materials requires improved conversion efficiency. This is governed by the dimensionless figure of merit $ZT = S^2\sigma T/\kappa$, where S, σ, T, and κ are the Seebeck coefficient, electrical conductivity, absolute temperature, and thermal conductivity, respectively. The thermal conductivity includes contributions from both electronic thermal conductivity (κ_e) and lattice thermal conductivity(κ_l) [2,3]. ZT thus consists of a combination of transport quantities. These quantities are generally correlated with each other in ways that work against high ZT. In particular, electrical conductivity and Seebeck coefficient are generally countercorrelated, and in addition it is difficult to achieve both high electrical conductivity and very low thermal conductivity. Nonetheless, there are a variety of approaches to improve thermoelectric performance. One approach is to enhance electrical transport performance by band engineering to decouple S and σ, for example through large band degeneracy (N_v) and/or anisotropic carrier pockets [4,5]. Another is to minimize the lattice thermal conductivity by forming a solid solution [6,7], nanostructuring [8], alloying [9,10], manipulation of grain boundaries [11,12], or seeking out compounds with intrinsically low lattice thermal conductivity originating from liquidlike atomic behavior [13], lone-pair electrons [14], or strong lattice anharmonicity [15,16].

Half-Heusler (HH) compounds are a relatively new class of promising thermoelectric materials with generally favorable thermodynamic and mechanical properties [17]. Importantly, HH compounds are a very large class of materials, providing a large space to search for desirable properties and for optimization. They often have large band degeneracies, which is a consequence of their high cubic crystal symmetry [18–21]. This can lead to favorable electrical properties due to the resulting decoupling of S and σ, particularly if the degenerate carrier pockets are also anisotropic, as is often the case. Interestingly, HH compounds have a wide range of lattice thermal conductivities. Nonetheless, these are generally higher than the lattice thermal conductivities of other state-of-the-art thermoelectrics. Therefore, reducing thermal conductivity is an important part of HH thermoelectric research.

*zzfeng@henu.edu.cn
†gfzhao@henu.edu.cn
‡singhdj@missouri.edu

 ©2022 American Physical Society

Alloying is widely used to suppress the propagation of heat-carrying phonons in these compounds. For example, the κ_l of FeNbSb is remarkably reduced by doping Ti atoms due to the enhanced point-defect scattering [22], and the thermal conductivity of TaFeSb-based (NbCoSn-based) systems is remarkably reduced by forming the $Ta_{0.84}Ti_{0.16}FeSb$ ($NbCo_{0.90}Ni_{0.10}Sn$) alloy [21,23,24]. However, while such defect engineering can reduce thermal conductivity, it also enhances electron scattering, leading to reduced electrical conductivity. Thus, it is challenging to identify alloys where the lattice conductivity is strongly reduced, while the electrical conductivity is weakly affected. It is therefore of considerable interest to investigate mechanisms for low thermal conductivity in HH materials and thereby identify HH compositions with intrinsically low thermal conductivity. This offers a path to high-performance thermoelectrics, specifically, if HH materials with intrinsically low thermal conductivity and also favorable electrical properties can be found.

Here we report a study of PCdNa (we list the atoms in the formula in this order to denote the sites that they occupy in the HH structure rather than using the IUPAC convention, NaCdP) based on first-principles density functional calculations. This is a compound that was predicted to be formable in the HH structure based on thermodynamic considerations [25], and which additionally is predicted to have an exceptionally low lattice thermal conductivity (2.27 W/mK at 300 K) [26]. The purpose of the present work is to better elucidate the origin of the low lattice thermal conductivity and to investigate the electronic and thermoelectric properties. We find the explanation for the low thermal conductivity in anharmonic effective rattling of the Cd ions within their cages. This is distinct from classical rattling that manifests itself in flat optical phonon modes intersecting the acoustic modes, but shares some of the same physics, specifically soft anharmonic phonons originating in a weakly bonded atom. In addition, we find favorable thermoelectric properties for *p*-type. These arise from multiple valence band pockets that are additionally anisotropic and corrugated. This leads to a decoupling of S and σ with ZT values that reach 0.8 at 300 K and 3.3 at 900 K for the optimum carrier concentration.

II. COMPUTATIONAL METHODS

A. Density functional theory calculations

The crystal structure optimization of PCdNa is carried out in the framework of density functional theory (DFT) as implemented in the Vienna *Ab initio* Simulation Package (VASP) [27]. The generalized gradient approximation (GGA) of Perdew-Burke-Ernzerhof is employed for the exchange-correlation potential [28]. We use the projector augmented wave method [29] for the electron-ion interactions. A plane-wave kinetic energy cutoff of 500 eV is used and the Brillouin zone (BZ) is sampled using a regular $15 \times 15 \times 15$ k-point mesh. The geometry is relaxed until the total energy is less than 10^{-8} eV. A $3 \times 3 \times 3$ supercell is used in the *ab initio* molecular dynamics (AIMD) calculations. These were done at temperatures of 300 and 900 K. Transport is studied for the optimized structure. Specifically, calculations are done with the full-potential linearized augmented plane wave (LAPW) implemented in the WIEN2k program package [30]. For this purpose, the Tran-Blaha modified Becke-Johnson (TB-mBJ) [31] potential is used. This generally gives band gaps for semiconductors in much better agreement with experiment than standard GGA functionals. Spin-orbit coupling (SOC) is included in these calculations. The computed electronic structures with the TB-mBJ functional and SOC is used to obtain electrical transport properties. The transport properties are obtained based on the semiclassical Boltzmann theory implemented in the BoltzTraP code [32] based on first-principles eigenvalues at approximately 50 000 k points and relaxation times obtained with the deformation potential, as below. The deformation potential method provides a computationally convenient method for approximating the relaxation time needed for transport calculations without doing full electron phonon calculations and has been widely used in thermoelectrics research [33–38].

B. Lattice thermal conductivity

The lattice thermal conductivity was obtained from first principles. Specifically, the lattice thermal conductivity κ_l can be calculated via the linearized Boltzmann equation [39] with harmonic and anharmonic interatomic force constants as the sum of contributions over all the phonon modes λ with branch p and wave vector q:

$$\kappa_l \equiv \kappa_{\alpha\alpha} = \frac{1}{NV}\sum_{\lambda}\frac{\partial f}{\partial T}\hbar\omega_\lambda v_\lambda^\alpha v_\lambda^\alpha \tau_\lambda, \tag{1}$$

where N is the number of uniformly spaced q points in the BZ, V is the volume of the unit cell, f is the Bose-Einstein distribution function depending on the phonon frequency ω_λ, and v_λ^α is the phonon velocity. The phonon lifetime τ_λ, an inverse of the total scattering rate, is determined by two processes: two-phonon scattering from isotopic disorder and three-phonon anharmonic scattering, which is a sum of the two-phonon isotopic scattering rate $1/\tau^{\text{iso}}$ and the three-phonon anharmonic scattering rate $1/\tau^{\text{anh}}$. $1/\tau^{\text{anh}}$ involves the sum over three-phonon transition probabilities $\Gamma^{\pm}_{\lambda\lambda'\lambda''}$, which can be calculated as

$$\Gamma^{\pm}_{\lambda\lambda'\lambda''} = \frac{\hbar\pi}{8N}\left\{\frac{2(f_{\lambda'}-f_{\lambda''})}{f_{\lambda'}+f_{\lambda''}+1}\right\} \times \frac{\delta(\omega_\lambda \pm \omega_{\lambda'} - \omega_{\lambda''})}{\omega_\lambda\omega_{\lambda'}\omega_{\lambda''}}|V^{\pm}_{\lambda\lambda'\lambda''}|^2, \tag{2}$$

where the upper (lower) row of curly brackets goes with the $+$ $(-)$ sign for absorption (emission) processes. The scattering matrix elements $V_{\lambda\lambda'\lambda''}$ are determined by the third-order interatomic force constants (IFCs).

The Phonopy package [40,41] is used for the harmonic second-order IFCs and the phonon dispersions. We use $4 \times 4 \times 4$ supercells (with 192 atoms in total) and $2 \times 2 \times 2$ k-point meshes for calculating the dynamical matrix. We impose an interaction range cutoff of 5.0 Å. Based on the harmonic phonon calculations, the Grüneisen parameters (γ) are calculated by the $\gamma_i = -\frac{V}{\omega_i}\frac{\partial\omega_i}{\partial V}$, in which the system volume is isotropically expanded by $+1\%$ from the DFT relaxed volume. In addition, the anharmonic third-order IFCs are

calculated using the same supercell and k meshes, as implemented in the thirdorder.py [42] code. The lattice thermal conductivities κ_l are then calculated by iteratively solving the linearized Boltzmann-Peierls transport equation via the SHENGBTE package [42,43]. A phonon momentum q mesh of $45 \times 45 \times 45$ is used in the calculation.

C. Electrical transport properties

The electrical transport parameters (S and σ/τ) of PCdNa can be obtained by solving the semiclassical Boltzmann transport equation, as implemented in the BoltzTraP code. To obtain σ, it is necessary to have the carrier relaxation time τ. The τ for the acoustic-phonon scattering is given by

$$\tau = \frac{2^{1/2}\pi\hbar^4\rho\upsilon_l^2}{3E_d^2(m^*k_BT)^{3/2}}\frac{F_0(\beta)}{F_{1/2}(\beta)}, \tag{3}$$

where υ_l is the sound velocity, E_d is the deformation potential constant, m^* is the conductivity transport effective mass, and ρ is the mass density. The transport effective mass can be calculated by $(m^*)^{-1} = \sigma/e^2\tau n$ where n is the carrier density [44], and can be obtained directly as a function of doping levels using the BOLTZTRAP code. $F_x(\beta) = \int_0^\infty \frac{E^x}{1+\exp(E-\beta)}dE$, where $\beta = (E_F/k_BT)$ is the reduced chemical potential. The bulk modulus (B) and shear modulus (G) can be used to obtain the υ_l by $\upsilon_l = \sqrt{\frac{B+4/3G}{\rho}}$, as described elsewhere [45]. The deformation potential E_d is defined as $E_d = \Delta E/(\frac{\Delta V}{V})$. The E_d for holes and electrons is calculated based on the energy changes of the valence-band maximum (VBM) and the conduction-band minimum (CBM) with volume change $\Delta V/V$. In addition, the electronic thermal conductivity can be obtained by $\kappa_e = L_0\sigma T$, where L_0 is the Lorenz number. It is determined by

$$L_0 = \left(\frac{k_B}{e}\right)^2\left\{\frac{(r+\frac{7}{2})F_{r+5/2}}{(r+\frac{3}{2})F_{r+1/2}} - \left[\frac{(r+\frac{5}{2})F_{r+3/2}}{(r+\frac{3}{2})F_{r+1/2}}\right]^2\right\}. \tag{4}$$

III. RESULTS AND DISCUSSION

A. Crystal structure and thermal stability

As mentioned, PCdNa was identified as a potential HH material based on thermodynamic considerations by Carrete and co-workers [25]. We note that there is a known ternary phase $NaCd_4P_4$ that could compete with PCdNa and prevent its formation [46,47]. We calculated the enthalpy of the decomposition of $NaCd_4P_3$ into Cd, PCdNa, and CdP_2. We find that this decomposition is favored by a very small but nonzero energy of 0.087 eV per formula unit of $NaCd_4P_3$. This implies that the HH phase can exist. While it may be that there are other presently unknown competing structures, this does suggest the potential for synthesizing PCdNa.

The HH structure is cubic with space group $F\bar{4}3m$. It consists of three interpenetrating face-centered cubic (fcc) sublattices and one vacant fcc sublattice, which if filled would yield the full-Heusler structure. The calculated lattice constant of PCdNa is $a = 6.445$ Å. P occupies site 4c (1/4, 1/4, 1/4), the Cd occupies 4a (0,0,0), and Na occupies 4b (1/2, 1/2, 1/2). In other words, the Cd and Na atoms form a NaCl rocksalt subunit, with half of the eight cube voids occupied by P atoms. The structure may also be viewed as a zinc-blende structure formed by P and Cd with Na filling atoms, or as a zinc blende formed by P and Na with Cd filling atoms.

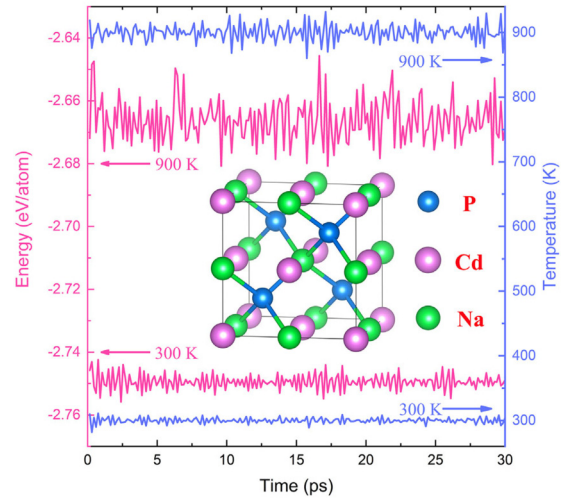

FIG. 1. AIMD evolution for the energy and temperature in bulk PCdNa at 300 and 900 K, respectively. The HH crystal structure is shown in the inset.

We now turn to the dynamical stability, which is essential for a material to be made. We investigated this by performing AIMD simulations at 300 and 900 K, as shown in Fig. 1. Clearly, the total energy and temperature have only small fluctuations during 30 ps AIMD simulations at 300 and 900 K, and there is no evidence of broken bonds or structural changes during the AIMD simulation. Thus, HH structure PCdNa is dynamically stable and can in principle exist not only at room temperature but also at elevated temperatures.

B. Phonons

The phonon dispersion curves together with the projected phonon density of states (PHDOS) are shown in Fig. 2. As in the case of the AIMD simulations, dynamical stability is found and, in particular, there are no imaginary frequency modes [40]. The modes are separated into three frequency

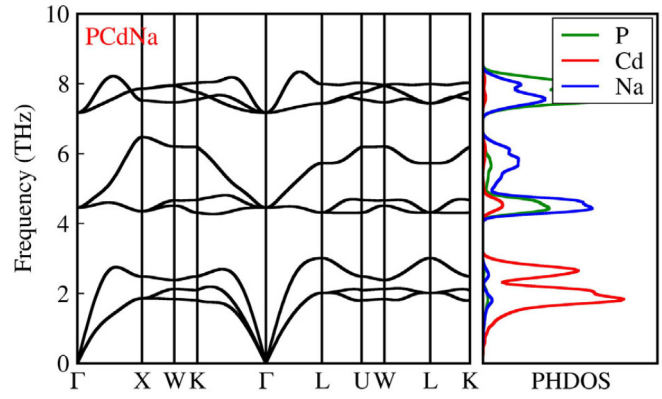

FIG. 2. Calculated phonon dispersion curves and phonon density of states for PCdNa.

ranges separated by full gaps. These are a lower acoustic set of three modes, a middle set of three modes, and an upper set of three modes. The longitudinal acoustic mode is much more strongly dispersive than the two transverse modes, as is seen along Γ–X and Γ–L in the plot. This is notable because the HH structure can be regarded as a filled zinc-blende structure that may be stabilized by covalent or ionic bonding. Covalent bonding is generally directional. This leads to closer dispersions of the transverse and longitudinal modes, which can lead to high thermal conductivity as in boron arsenide [48,49]. In any case, the substantially more dispersive longitudinal acoustic (LA) mode relative to the transverse acoustic branches indicates that it is likely to be the main heat carrying branch, characteristic of more ionic materials.

Importantly, the LA branch is gapped. This is seen, for example, along Γ–X, where the branch disperses strongly up to approximately half way to X, and then flattens and turns down. Meanwhile, the top branch in the middle set of modes beginning from disperses upwards towards X with an upward curvature. Thus, there is an anticrossing of these branches. The lowest set of modes gives two main peaks in the phonon density of states. The lower peak comes from flattening of the transverse branches near the zone boundary, while the upper peak is from the flattening of the heat-carrying longitudinal branch due to the anticrossing mentioned above.

The PHDOS shows that flat, low-energy acoustic modes (around 2.5 THz) are dominated by Cd atoms, whereas the optical branches are governed by P and Na atoms. The avoided crossing of the acoustic and the optical phonons is an indication of an effective atomic rattling. Rattling behavior has been observed in skutterudites and clathrates, which are well known for their very low lattice thermal conductivity. In those materials the so-called guest atoms rattle in the host cage substructures and scatter heat-carrying phonons through their interaction with the host [50–53]. Here, there is an underbonded Cd atom that results in an effective rattling but the coupling to the host lattice is strong enough that it does not lead to very flat optical branches intersecting the acoustic branches, and in fact the acoustic modes in PCdNa have strong Cd character themselves.

We calculated the harmonic second-order IFCs between Cd-P, Cd-Na, and P-Na, respectively. The IFCs provide insight into the bond strengths and interaction of each atom with the other atoms in the lattice. The IFCs maximum value of P-Na is larger than that of Cd-P and Cd-Na, as discussed below. This means that the Cd atom is relatively weakly bonded as compared with the P and Na atoms. This supports the possibility that Cd serves as a rattler in PCdNa. Within an ionic picture, HH structure PCdNa would contain anionic P^{3-}, which is a very large species, and cationic Cd^{2+} and Na^{+}. In the HH structure each Cd and Na is coordinated by four P at a distance of $a\sqrt{3}/4 = 2.791$ Å. The Shannon ionic crystal radii [54] for fourfold coordinated Na^{+} is 1.13 Å, while that for Cd^{2+} is 0.92 Å, which is significantly smaller. It should be noted that the compound may not be fully ionic and, in particular, Cd may be expected to have some covalency. However, covalent bonds are generally shorter than ionic bonds. The shortest Cd-P bond length in Cd_3P_2 is 2.504 Å, while in Na_3P the shortest Na-P bond length is 2.859 Å, which is substantially longer [55,56].

This implies that the structural constraints of the HH structure where the $A-B$ and $A-C$ bond lengths are constrained to be the same, leads to a substantial underbonding of Cd in PCdNa. This is supported by the IFCs. The maximum value of the IFC for P-Na is 0.539 eV/Å^2, as compared to Cd-P, with a maximum IFC of 0.184 eV/Å^2 and Cd-Na with a maximum IFC of 0.227 eV/Å^2. The weak bonding of Cd compared with Na is particularly notable considering that it is opposite to the usual crystal chemical trend where the divalent atom (Cd in PCdNa) is more strongly bonded than the monovalent atom (Na).

In addition, we have developed an atom specific effective spring constant ($k = \bar{\omega}^2 m$) based on analysis of the PHDOS of a database of HH materials, to characterize effective binding forces as related to thermal conductivity, and established a descriptor ($k_{\min}/k_{\max}$) to characterize the bond frustration and anharmonicity [26]. The calculated effective spring constant k (N/m) of each atom and the ratio between the minimum to maximum spring constant in PCdNa is shown in Table I. It is clear that PCdNa has a small ratio of $k_{\min}$ to $k_{\max}$. This means that at least one atom is weakly bonded. Compared with the k value of P, the small k value of Cd means that the Cd atom is weakly bonded with P and Na atoms. This weak bonding is a feature of classical rattling. It is also seen that Na also has a relatively low k as compared to P, although this is much higher than the Cd k. However, the light mass of Na leads to higher frequency optical modes as compared to Cd.

There is also avoided crossing of the acoustic and the optical phonons. The phonon density of states shows a mixing of character. In particular, there is significant Cd character in the lower set of optical branches, although these modes in the second set have strong Na and P character. This avoided crossing leads to a flattening of the LA branch at ∼2 THz. This strong anticrossing means that while Cd is relatively underbonded in the lattice, it does interact with the atoms in its cage at a level sufficient to affect the phonons and thus the thermal conductivity. This type of interaction leading to a two-peak structure in the PHDOS was also noted as an important aspect of filled skutterudites [57].

In addition to this effective rattling behavior of Cd, HH structure PCdNa has a relatively soft lattice that favors low thermal conductivity. Phonon group velocities are shown in Fig. 3(a). The maximum values of group velocities are no more than 1650 and 2160 m/s for the TA and LA branches, respectively. These results are comparable to those of good TE with low lattice thermal conductivity, such as SnSe (κ_l = 0.5 W/mK at 300 K, $\upsilon_{TA} = 1194$ m/s, $\upsilon_{LA} = 2117$ m/s) [58] and PbTe (κ_l = 2.1 W/mK at 300 K, $\upsilon_{TA} = 1610$ m/s, $\upsilon_{LA} = 3596$ m/s) [59,60]. Finally, it may be noted from the PHDOS that while the two upper groups of modes have mixed Na and P character, the highest frequency set, centered around 8 THz, are more P derived, while the lower set of optical branches centered around 5 THz is more Na derived. This is in contrast to the expectation from the atomic masses ($M_{\mathrm{Na}} = 22.99$, $M_{\mathrm{P}} = 30.98$), indicating that the P is subject to substantially stiffer force constants than Na. It may reflect an expected large size of the P^{3-} anion and resulting direct P-P repulsion that would expand the lattice and lead to underbonding of the cations. This is clearly seen as well in the effective force constants from the phonon density of states in Table I.

TABLE I. Effective spring constant k (N/m) for each atom, and the ratio between the minimum to maximum spring constant in PCdNa, and the average transverse (TA/TA′), longitudinal (LA), and total Grüneisen parameters ($\bar{\gamma}_{TA/TA'/LA/\text{Total}}$).

Compound	k_1 (P)	k_2 (Cd)	k_3 (Na)	$k_{\min}/k_{\max}$	$\bar{\gamma}_{TA}$	$\bar{\gamma}_{TA'}$	$\bar{\gamma}_{LA}$	$\bar{\gamma}_{\text{Total}}$
PCdNa	90.68	41.24	47.91	0.45	5.13	3.87	3.37	4.19

Another factor of importance is the anharmonicity. Typically, underbonding or nearness to structural instabilities leads to high anharmonicity, which favors low thermal conductivity. We calculated the Grüneisen parameters of the modes, shown on dispersion curves of PCdNa along high-symmetry directions in Fig. 3(b). Usually, a large Grüneisen parameter reflects a strong crystal anharmonicity [61–63]. To quantitatively evaluate the anharmonicity, the average transverse (TA and TA′, for the lowest and second-lowest transverse), longitudinal (LA), and total Grüneisen parameters ($\bar{\gamma}_{TA/TA'/LA/\text{Total}}$) are calculated by $\bar{\gamma} = \sqrt{\langle \gamma_i^2 \rangle}$, and they are listed in Table I. The average acoustic Grüneisen parameters are $\bar{\gamma}_{TA} = 5.13$, $\bar{\gamma}_{TA'} = 3.87$, $\bar{\gamma}_{LA} = 3.37$, and $\bar{\gamma}_{\text{Total}} = 4.19$, respectively. The Grüneisen parameters of PCdNa are similar to those of ultralow thermal conductivity SnSe ($\bar{\gamma}_{TA} = 5.1$, $\bar{\gamma}_{TA'} = 1.1$, $\bar{\gamma}_{LA} = 5.9$, and $\bar{\gamma}_{\text{Total}} = 4.1$) [58]. The low acoustic phonon velocities and the strong anharmonicity may be expected to lead to low lattice thermal conductivity for PCdNa.

Finally, the phonon dispersion shows that the TA and LA branches are separated and, in particular, the TA phonons have much lower velocity than the LA phonons. This separation is a reflection of a more ionic bonding nature. It is in contrast to materials with strong directional covalent bonding, which will lead to stiffer shear modes, higher transverse velocities, and thus less separation of the TA and LA branches. Importantly, the separation of the TA and LA branches can enhance the scattering phase space. Detailed thermal conductivity calculations show that PCdNa has strong three acoustic phonons scattering. This also contributes to a low lattice thermal conductivity.

Turning to the calculations of the thermal conductivity, we find that compared with other excellent HH thermoelectric materials, PCdNa has a particularly low lattice thermal conductivity (2.61 W/mK at 300 K), and decreases with temperature, as shown in Fig. 4(a). The cumulative thermal conductivity as a function of frequency calculated at 300 K is shown in Fig. 4(b). This increases rapidly in the low-frequency acoustic modes of 1–3 THz, and this part of the phonons contributes 92% of the lattice thermal conductivity. The optic modes therefore contribute very little to the thermal conductivity. Furthermore, the thermal conductivity practically saturates at the frequency where the LA branch becomes flat.

C. Electronic structure and electrical transport

TE performance depends both on a low lattice thermal conductivity and favorable electrical transport properties. The electrical transport properties of a compound depend strongly on its electronic structures. The electronic band structure of PCdNa is shown in Fig. 5(a). PCdNa is found to be a semiconductor with a 1.13 eV direct band gap at the Γ point. From the electronic density of states of Fig. 5(b), the valence band originates from the P-p and Cd-d states, and the conduction band is primarily dominated by the P-p and Cd-s states with a contribution of Cd-d states. There is very little Na character around the band edges. This reflects the ionic character of Na, so that the main Na character is at higher energy.

It may be noted that the CBM comes from dispersive states while the bands around the VBM are considerably less dispersive. Thus, the band effective mass of p-type PCdNa is heavier than that of n-type; the heavier effective mass is expected to

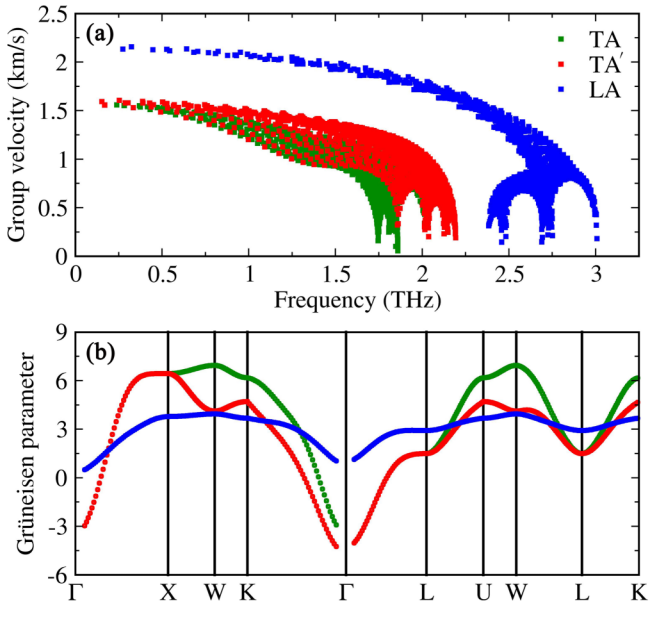

FIG. 3. (a) The group velocity of different phonon modes as a function of frequency for PCdNa. (b) The calculated Grüneisen parameter dispersion for PCdNa. The TA, TA′, and LA modes are shown as green, red, and blue lines, respectively.

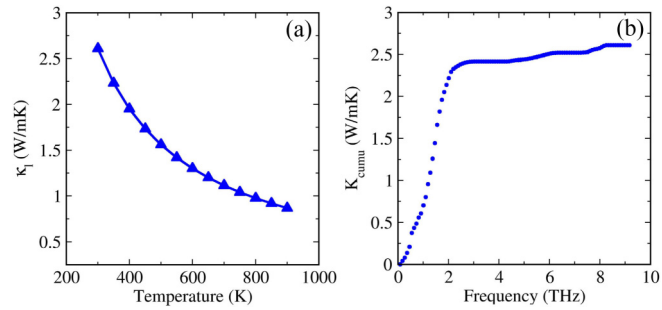

FIG. 4. (a) The lattice thermal conductivity as a function of temperature; (b) the cumulative lattice thermal conductivity in the PCdNa at 300 K as a function of frequency at 300 K.

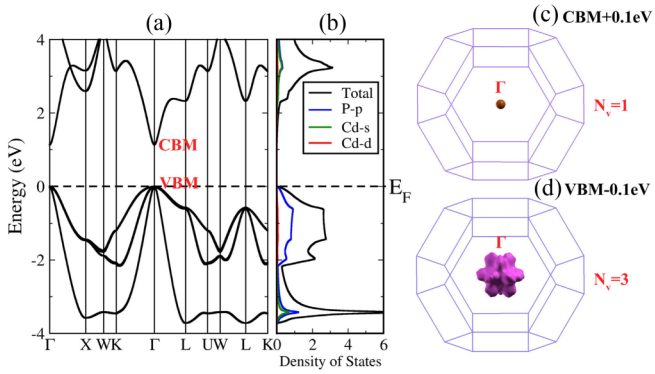

FIG. 5. (a) Band structures of PCdNa as determined using the modified Becke-Johnson potential and carrier pocket shapes as given by isosurfaces. (b) Projected density of states of PCdNa. Here the projections are onto LAPW spheres. This underestimates the contributions from extended orbitals that extend outside the spheres, as for the P p orbitals. (c) Carrier pocket visualization using band energy isosurfaces 0.1 eV above the conduction-band minimum for electrons and (d) 0.1 eV below the valence-band maximum for holes.

lead to a smaller electrical conductivity of p-type than that of the n-type one, as shown in Figs. 6(a) and 6(b). However, the transport and density of states effective mass can differ with band structures that are not well characterized with a single parabolic band (SPB). As mentioned, these differences can lead to enhancement of the TE performance by decoupling

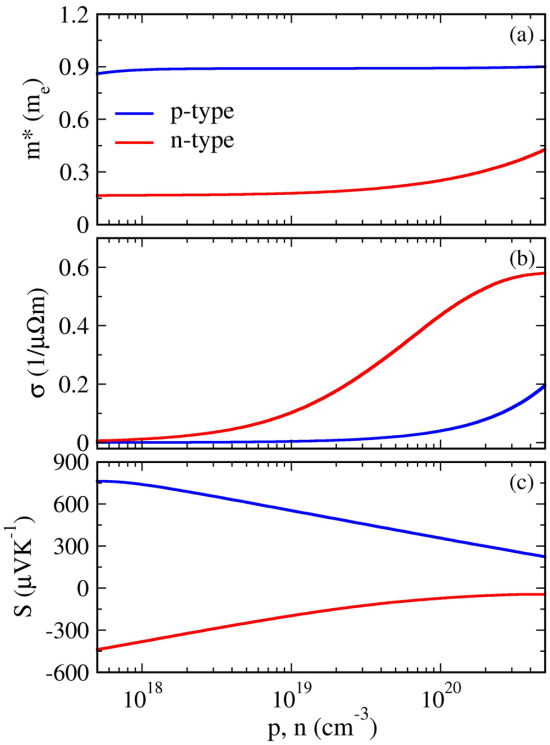

FIG. 6. Calculated electrical transport properties for PCdNa at 900 K: (a) transport effective mass m^*, (b) electrical conductivity σ, and (c) Seebeck coefficient S.

TABLE II. Parameters entering the deformation potential calculation. These are the calculated bulk modulus (B) and shear modulus (G), density (ρ), deformation potential (E_d) for holes and electrons, and longitudinal sound velocity (υ_l) for PCdNa.

Quantity	Value
Bulk modulus, B	43.01 GPa
Shear modulus, G	26.55 GPa
Density, ρ	4127 kg/m^3
Hole deformation potential, $E_{d\ \text{holes}}$	7.021 eV
Electron deformation potential, $E_{d\ \text{electrons}}$	10.347 eV
Longitudinal velocity, υ_l	4359 m/s

the SPB relationship between conductivity and the Seebeck coefficient [64].

One important factor is the total number of independent carrier pockets or valleys in the BZ [5,65]. The N_v ($N_v = 3$) of the valence band is higher than that of the conduction band ($N_v = 1$). As mentioned, there is an effective degeneracy of $N_v = 3$ for valence band maximum. This arises from a twofold degenerate band maximum at Γ, with a very strong k-dependent corrugation due to the interaction of these two bands, and a light hole band separated by a very small spin-orbit gap of 0.03 eV. Thus at temperatures somewhat above ambient these bands become effectively degenerate, and the light hole band and the heavy hole bands are both occupied at doping levels of interest for thermoelectricity. This heavy-light band combination is favorable for thermoelectric performance as the heavy bands enhance the Seebeck coefficient, while the light band improves conductivity. This heavy-light mixture plus the corrugation of the heavy bands as seen in the isosurface visualization favor thermoelectric performance. A key aspect is therefore the small spin-orbit splitting, which arises because neither Cd nor Na is a p element and P has a relatively low atomic number. In addition, carrier pocket shapes are of importance, since anisotropic carrier pockets can also provide decoupling. We plot the carrier pocket shapes as given by isoenergy surfaces 0.1 eV above the CBM for electrons and 0.1 eV below the VBM for holes, as shown in Figs. 5(c) and 5(d), respectively. The hole pockets have a corrugated anisotropic shape, different from the electron pockets, which are close to spherical. The complex shape of the hole pockets, which is a consequence of the band degeneracy, favors thermoelectric performance [66,67]. The effect is seen in the rapid onset of the electronic density of states at the valence-band edge. This leads to a large S for p-type PCdNa without a corresponding large reduction of the electrical conductivity, as shown in Fig. 6(c).

We calculated the effective transport mass, m^*, σ and S at 900 K using the BOLTZTRAP code. The results are shown in Fig. 6. From Fig. 6(a), the transport effective mass of p-type PCdNa is larger than that of n-type. The larger transport effective mass will lead a lower electrical conductivity, but as discussed below, the enhanced Seebeck coefficient compensates for this. The other quantities entering the deformation potential calculation are given in Table II. Figure 6(b) shows the electrical conductivity, while the Seebeck coefficient is give in Fig. 6(c). As seen, the Seebeck coefficient of p-type

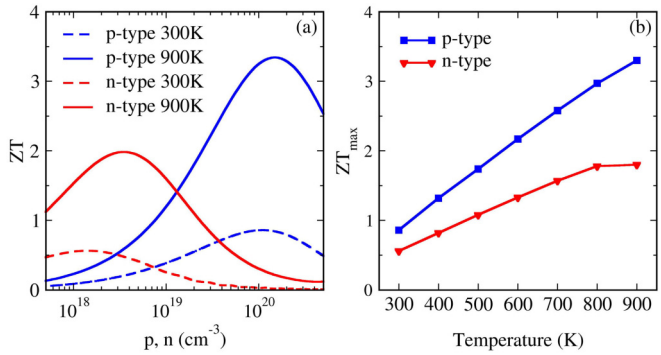

FIG. 7. (a) The calculated ZT values of PCdNa as a function of carrier concentration at 300 and 900 K. (b) Temperature-dependent ZT values for both n-type and p-type.

PCdNa is significantly larger than that of n-type. Combining these it is seen that the TE performance for p-type is superior to that for n-type.

D. Thermoelectric performance

We can obtain the ZT values of HH structure PCdNa from the electrical and thermal transport properties. The calculated ZT values at 300 and 900 K are presented in Fig. 7(a). At room temperature, the peak ZT of p-type and n-type are approximately 0.86 and 0.56, and the corresponding optimum carrier concentrations are 1.08×10^{20} cm^{-3} and 1.69×10^{18} cm^{-3}, respectively. The highest ZT values of p-type and n-type PCdNa at 900 K are about 3.3 and 2.0, and the corresponding carrier concentrations are 1.49×10^{20} cm^{-3} and 3.42×10^{18} cm^{-3}, respectively. We note that when the ZT value of p-type PCdNa reaches the maximum, the optimal carrier concentration at a temperature of 300 K is reasonably similar to the carrier concentration of 900 K. This is favorable for producing devices with wide operating temperature ranges. The maximum ZT value as a function of temperature from 300 to 900 K is shown in Fig. 7(b). The highest ZT values of p-type and n-type PCdNa are approximately 2.2 and 1.3 at a medium temperature of 600 K. Therefore, the PCdNa is a promising thermoelectric material. This suggests experimental work to synthesize the phase and characterize its transport properties. The favorable thermoelectric properties are the consequence of a very low thermal conductivity and favorable electrical properties particularly for p-type.

IV. SUMMARY AND CONCLUSIONS

We investigated the lattice thermal conductivity, electronic structures, and electrical transport properties of the half-Heusler compound PCdNa using density functional theory. The results show that the Cd atoms serve as generalized rattlers in the cages formed by neighboring P anions, and that this leads to an exceptionally low lattice thermal conductivity (2.61 W/mK at 300 K) for a HH compound. Specifically, the Cd atoms are underbonded, as reflected in calculated IFCs and effective spring constants extracted from the phonon dispersions. This is a consequence of bond length constraints of the HH structure and leads to soft anharmonic phonons that lower the thermal conductivity. In addition, the large band degeneracy and corrugated Fermi surface of a valence band of p-type PCdNa are favorable for the electrical transport properties. Owing to the low lattice thermal conductivity and the good electrical transport properties, we obtain the highest ZT value of 3.3 for p-type at 900 K. Therefore, our work suggests exploration of p-type PCdNa as a promising thermoelectric material, and provides insights into the nature of rattling for the reduction of thermal conductivity in half-Heusler materials.

ACKNOWLEDGMENTS

The work was supported by National Natural Science Foundation of China, Award No. 12047518, and the China Postdoctoral Science Foundation (2020TQ0088, 2021M690906).

[1] A. F. Ioffe, L. Stil'Bans, E. Iordanishvili, T. Stavitskaya, A. Gelbtuch, and G. Vineyard, Phys. Today **12**(5), 42 (1959).
[2] C. Wood, Rep. Prog. Phys. **51**, 459 (1988).
[3] A. Roy, Phys. Rev. B **93**, 100101(R) (2016).
[4] Q. Zhang, Q. Song, X. Wang, J. Sun, Q. Zhu, K. Dahal, X. Lin, F. Cao, J. Zhou, S. Chen *et al.*, Energy Environ. Sci. **11**, 933 (2018).
[5] Y. Pei, X. Shi, A. LaLonde, H. Wang, L. Chen, and G. J. Snyder, Nature (London) **473**, 66 (2011).
[6] S. Guo, K. Yang, Z. Zeng, and Y. Zhang, Phys. Chem. Chem. Phys. **20**, 14441 (2018).
[7] A. Zevalkink, S. Chanakian, U. Aydemir, A. Ormeci, G. Pomrehn, S. Bux, J.-P. Fleurial, and G. J. Snyder, J. Phys.: Condens. Matter **27**, 015801 (2015).
[8] B. Poudel, Q. Hao, Y. Ma, Y. Lan, A. Minnich, B. Yu, X. Yan, D. Wang, A. Muto, D. Vashaee *et al.*, Science **320**, 634 (2008).
[9] C. Yu, T.-J. Zhu, R.-Z. Shi, Y. Zhang, X.-B. Zhao, and J. He, Acta Mater. **57**, 2757 (2009).
[10] S. Sakurada and N. Shutoh, Appl. Phys. Lett. **86**, 082105 (2005).
[11] H. Mun, S.-M. Choi, K. H. Lee, and S. W. Kim, ChemSusChem **8**, 2312 (2015).
[12] B.-Z. Tian, J. Chen, X.-P. Jiang, J. Tang, D.-L. Zhou, Q. Sun, L. Yang, and Z.-G. Chen, ACS Appl. Mater. Interfaces **13**, 50057 (2021).
[13] H. Kim, S. Ballikaya, H. Chi, J.-P. Ahn, K. Ahn, C. Uher, and M. Kaviany, Acta Mater. **86**, 247 (2015).
[14] Z. Feng, T. Jia, J. Zhang, Y. Wang, and Y. Zhang, Phys. Rev. B **96**, 235205 (2017).
[15] T. Jia, G. Chen, and Y. Zhang, Phys. Rev. B **95**, 155206 (2017).
[16] Y. Fu, X. He, L. Zhang, and D. J. Singh, Phys. Rev. B **97**, 024301 (2018).
[17] H. Zhu, R. He, J. Mao, Q. Zhu, C. Li, J. Sun, W. Ren, Y. Wang, Z. Liu, Z. Tang *et al.*, Nat. Commun. **9**, 2497 (2018).

[18] G. Rogl, A. Grytsiv, M. Gürth, A. Tavassoli, C. Ebner, A. Wünschek, S. Puchegger, V. Soprunyuk, W. Schranz, E. Bauer, H. Muller *et al.*, Acta Mater. **107**, 178 (2016).
[19] H. Shi, W. Ming, D. S. Parker, M.-H. Du, and D. J. Singh, Phys. Rev. B **95**, 195207 (2017).
[20] S. Li, H. Zhu, J. Mao, Z. Feng, X. Li, C. Chen, F. Cao, X. Liu, D. J. Singh, Z. Ren, and Q. Zhang, ACS Appl. Mater. Interfaces **11**, 41321 (2019).
[21] H. Zhu, J. Mao, Y. Li, J. Sun, Y. Wang, Q. Zhu, G. Li, Q. Song, J. Zhou, Y. Fu *et al.*, Nat. Commun. **10**, 1 (2019).
[22] C. Fu, T. Zhu, Y. Liu, H. Xie, and X. Zhao, Energy Environ. Sci. **8**, 216 (2015).
[23] R. Yan, R. Xie, W. Xie, C. Shen, W. Li, B. Balke, S. Yoon, H. Zhang, and A. Weidenkaff, ACS Appl. Mater. Interfaces **13**, 34533 (2021).
[24] R. He, L. Huang, Y. Wang, G. Samsonidze, B. Kozinsky, Q. Zhang, and Z. Ren, APL Mater. **4**, 104804 (2016).
[25] J. Carrete, W. Li, N. Mingo, S. Wang, and S. Curtarolo, Phys. Rev. X **4**, 011019 (2014).
[26] Z. Feng, Y. Fu, Y. Zhang, and D. J. Singh, Phys. Rev. B **101**, 064301 (2020).
[27] G. Kresse and J. Furthmüller, Comput. Mater. Sci. **6**, 15 (1996).
[28] J. P. Perdew, K. Burke, and M. Ernzerhof, Phys. Rev. Lett. **77**, 3865 (1996).
[29] P. E. Blöchl, Phys. Rev. B **50**, 17953 (1994).
[30] K. Schwarz, P. Blaha, and G. K. Madsen, Comput. Phys. Commun. **147**, 71 (2002).
[31] F. Tran and P. Blaha, Phys. Rev. Lett. **102**, 226401 (2009).
[32] G. K. Madsen and D. J. Singh, Comput. Phys. Commun. **175**, 67 (2006).
[33] H. Wang, Y. Pei, A. D. LaLonde, and G. J. Snyder, Proc. Natl. Acad. Sci. USA **109**, 9705 (2012).
[34] T. H. Liu, J. Zhou, M. Li, and G. Chen, Proc. Natl. Acad. Sci. U.S.A. **115**, 879 (2018).
[35] A. J. Hong, L. Li, R. He, J. J. Gong, Z. B. Yan, K. F. Wang, J. M. Liu, and Z. F. Ren, Sci. Rep. **6**, 22778 (2016).
[36] Y. Sheng, Y. Wu, J. Yang, W. Lu, P. Villars, and W. Zhang, npj Comput. Mater. **6**, 171 (2020).
[37] R. Li, X. Li, L. Xi, J. Yang, D. J. Singh, and W. Zhang, ACS Appl. Mater. Interfaces **11**, 24859 (2019).
[38] B. Kozinsky and D. J. Singh, Annu. Rev. Mater. Res. **51**, 565 (2021).
[39] M. Omini and A. Sparavigna, Phys. Rev. B **53**, 9064 (1996).
[40] A. Togo and I. Tanaka, Scr. Mater. **108**, 1 (2015).
[41] A. Togo, F. Oba, and I. Tanaka, Phys. Rev. B **78**, 134106 (2008).
[42] W. Li, J. Carrete, N. A. Katcho, and N. Mingo, Comput. Phys. Commun. **185**, 1747 (2014).
[43] W. Li, L. Lindsay, D. A. Broido, D. A. Stewart, and N. Mingo, Phys. Rev. B **86**, 174307 (2012).
[44] Z. M. Gibbs, F. Ricci, G. Li, H. Zhu, K. Persson, G. Ceder, G. Hautier, A. Jain, and G. J. Snyder, npj Comput. Mater. **3**, 8 (2017).
[45] O. L. Anderson, J. Phys. Chem. Solids **24**, 909 (1963).
[46] C. Grotz, M. Baumgartner, K. M. Freitag, F. Baumer, and T. Nilges, Inorg. Chem. **55**, 7764 (2016).
[47] A. M. Medina-Gonzalez, P. Yox, Y. Chen, M. A. S. Adamson, M. Svay, E. A. Smith, R. D. Schaller, A. J. Rossini, and J. Vela, ACS Mater. Au **1**, 130 (2021).
[48] L. Lindsay, C. Hua, X. Ruan, and S. Lee, Mater. Today Phys. **7**, 106 (2018).
[49] L. Lindsay, D. A. Broido, and T. L. Reinecke, Phys. Rev. Lett. **111**, 025901 (2013).
[50] J. Dong, O. F. Sankey, and C. W. Myles, Phys. Rev. Lett. **86**, 2361 (2001).
[51] Y. He and G. Galli, Nano Lett. **14**, 2920 (2014).
[52] G. Nolas, J. Cohn, G. Slack, and S. Schujman, Appl. Phys. Lett. **73**, 178 (1998).
[53] J. L. Cohn, G. S. Nolas, V. Fessatidis, T. H. Metcalf, and G. A. Slack, Phys. Rev. Lett. **82**, 779 (1999).
[54] R. D. Shannon, Acta Crystallogr., Sect. A: Found. Adv. **32**, 751 (1976).
[55] I. E. Zanin, K. B. Aleinkova, M. Y. Antipin, and M. M. Afanasiev, J. Struct. Chem. **47**, 78 (2006).
[56] Y. Dong and F. J. DiSalvo, Acta Crystallogr., Sect. E: Struct. Rep. Online **61**, i223 (2005).
[57] J. L. Feldman, D. J. Singh, I. I. Mazin, D. Mandrus, and B. C. Sales, Phys. Rev. B **61**, R9209(R) (2000).
[58] L.-D. Zhao, S.-H. Lo, Y. Zhang, H. Sun, G. Tan, C. Uher, C. Wolverton, V. P. Dravid, and M. G. Kanatzidis, Nature (London) **508**, 373 (2014).
[59] Z. Tian, J. Garg, K. Esfarjani, T. Shiga, J. Shiomi, and G. Chen, Phys. Rev. B **85**, 184303 (2012).
[60] G. Ding, J. Carrete, W. Li, G. Gao, and K. Yao, Appl. Phys. Lett. **108**, 233902 (2016).
[61] Y. Zhang, E. Skoug, J. Cain, V. Ozoliņš, D. Morelli, and C. Wolverton, Phys. Rev. B **85**, 054306 (2012).
[62] Y. Xiao, C. Chang, Y. Pei, D. Wu, K. Peng, X. Zhou, S. Gong, J. He, Y. Zhang, Z. Zeng, and L.-D. Zhao, Phys. Rev. B **94**, 125203 (2016).
[63] T. Jia, Z. Feng, S. Guo, X. Zhang, and Y. Zhang, ACS Appl. Mater. Interfaces **12**, 11852 (2020).
[64] G. Xing, J. Sun, Y. Li, X. Fan, W. Zheng, and D. J. Singh, Phys. Rev. Mater. **1**, 065405 (2017).
[65] Z. Feng, X. Zhang, Y. Wang, J. Zhang, T. Jia, B. Cao, and Y. Zhang, Phys. Rev. B **99**, 155203 (2019).
[66] X. Chen, D. Parker, and D. J. Singh, Sci. Rep. **3**, 3168 (2013).
[67] N. A. Mecholsky, L. Resca, I. L. Pegg, and M. Fornari, Phys. Rev. B **89**, 155131 (2014).